batteries

Article

Processing of Aqueous Graphite–Silicon Oxide Slurries and Its Impact on Rheology, Coating Behavior, Microstructure, and Cell Performance

Peter Haberzettl [1,*], Nicholas Filipovic [1], Dragoljub Vrankovic [1] and Norbert Willenbacher [2]

[1] Mercedes-Benz Group AG—RD/EBZ Zelltechnologie 1, Mercedesstr. 120, 70372 Stuttgart, Germany
[2] Institute of Mechanical Process Engineering and Mechanics—Applied Mechanics Group, Karlsruhe Institute of Technology (KIT), Gotthard-Franz-Str. 3, 76131 Karlsruhe, Germany; norbert.willenbacher@kit.edu
* Correspondence: peter.haberzettl@mercedes-benz.com

Abstract: The mixing process is the basis of the electrode microstructure, which defines key cell performance indicators. This work investigated the effects of varying the energy input within the mixing procedure on slurry rheology, coating behavior, mechanical and electrical properties of dry electrodes and electrochemical performance of cells fabricated from these negative electrodes. Energy input differences were achieved by varying the solids content within the mixing procedure; however, the final total solids content of the slurries was always the same. The slurries, produced with graphite and silicon oxide as active materials and carboxymethylcellulose (CMC) and styrene-butadiene rubber as binders, showed large differences in flow behavior which were explained by changes in CMC adsorption and mechanical degradation because of increasing energy input. Low shear viscosity and the degree of shear thinning decreased with increasing energy input, resulting in a narrower stability window for slot-die coating. The resistance between the electrode and current collector decreased as more CMC was adsorbed on the active material. Electrode adhesion drastically dropped at the highest energy input, presumably due to a change in SBR distribution. Despite these variations, all fabricated pouch cells demonstrated excellent electrochemical performance and a slight trend of increased charge capability was observed in cells prepared with higher energy input.

Keywords: mixing; slurry; rheology; polymer; CMC; adsorption; mechanical degradation; coating; negative electrode; lithium-ion cell

1. Introduction

Lithium-ion batteries are one of the key technologies in the global effort to reduce carbon emissions. This leads to a growing demand for lithium-ion cells (LICs) with advanced high-performance active materials (AMs) and well-managed production processes [1]. Within LIC production, the first and also product-defining step is the mixing of electrode suspensions, the so-called slurries [2–6]. These suspensions are used to make electrodes by coating them onto a metal current collector foil. After drying, the electrodes are compressed and cut into the desired shape for downstream processing into cells [7,8].

The slurry typically consists of an electrochemical AM, a conductive additive, a binder and a solvent. Each of these components has a specific purpose. The AM is the major component of the solid fraction and defines the polarity of the subsequent electrode and its electrochemical characteristics. To name a few, typical AMs in positive electrodes are metal oxides such as lithium cobalt (III) oxide (LCO), lithium nickel manganese cobalt oxide (NCM) or polyanionic compounds such as lithium iron phosphate (LFP). Negative electrodes use AMs such as lithium titanium oxide (LTO), natural or synthetic graphite (Gr), silicon or silicon-based compounds such as silicon oxide (SiO_x). A comprehensive review of AMs in LICs is given in [9]. Due to recent advances, AMs containing silicon are becoming more prominent in improving the energy density of the cell [10–12]. However,

compositions with silicon still struggle with cyclability, hysteresis, high changes in volume during lithiation and delithiation, just to name some, and are often used in combination with Gr to mitigate these issues [13–15]. Conductive additives improve the electronic conductivity of electrodes, where particulate carbons such as CB are widely used. They have high BET surface areas with a primary particle size in the nanometer range. More performance-oriented electrode compositions use fiber-like or tubular carbon materials, e.g., multi-wall or single-wall carbon nanotubes, but these are expensive [16]. The role of the binder within the electrode is very diverse: the dissolved binder defines the flow behavior of the slurry, stabilizes the suspension and, once dried, provides mechanical strength to the electrode, which ultimately affects the cycle life of the LIC [17,18]. In addition, adsorbing binders such as CMC can act as dispersing agents and provide steric stabilization to the slurry [19,20]. When CMC is used as a binder, a second polymer is needed to provide adhesion to the current collector and often styrene-butadiene rubber (SBR) is used for this purpose [21]. In conventional slurries, N-methyl-2-pyrrolidone (NMP) or water is used as the solvent. For industrial applications, it is desirable to keep the amount of solvent as low as possible, as the evaporation process is energy consuming and therefore expensive; furthermore, the use of solvents like NMP should be reduced due to their hazardous nature [22]. For this reason, the compositions studied here have a rather high total solids content (TSC).

Due to the physical and chemical diversity of materials, slurries come in many different consistencies. The key factors of a "good" slurry are a well-dispersed AM and conductive additive fraction, meaning the AM fraction has few to none agglomerates or aggregates remaining in the slurry and the conductive additives are dispersed to form a conductive network [23]. Furthermore, flow behavior has to be adjusted to guarantee stable processing conditions, particularly in the widely used slot-die coating application [24]. To achieve the desired quality criteria, a great deal of effort goes into the development of good mixing procedures, especially when scaling up from the laboratory to the plant scale. Some of the most prominent mixing process design considerations in the literature are steps such as dry blending of CB and AM, wet predispersion of conductive additives and mixing or kneading at high solids content [2–6,25–27]. However, while these processes are often the subject of comparison, variations within the process have rarely been the subject of research.
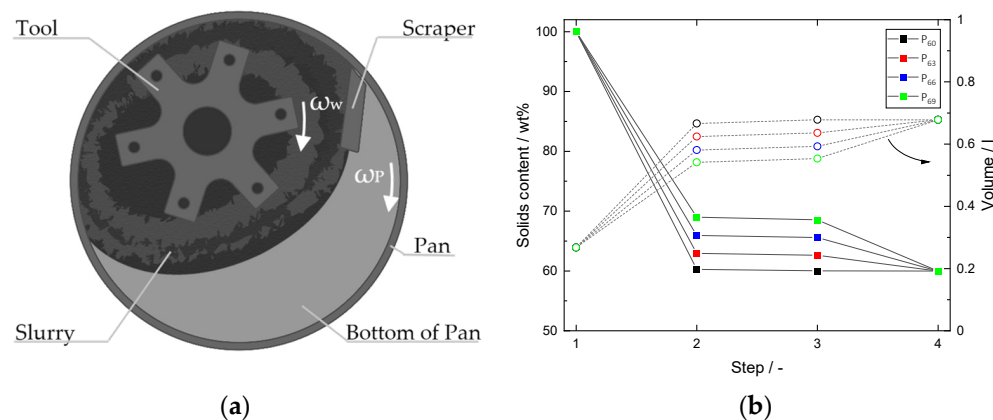
To gain a better understanding regarding the effect of small variations, such as adding more or less solvent during the mixing procedure, aqueous slurries (Gr-SiO$_x$) with the same composition were made using an industrially relevant intensive mixer. Varying the solids content during mixing resulted in a significant change in energy input, and it will be shown that this had a major effect on the mechanical degradation of CMC, used here as a binder together with SBR, and its absorption on the surface of AM particles. This in turn changes the flow behavior of the slurry dramatically and we thoroughly investigated how this affects coatability on a prototypical slot-die roll-to-roll coater. The operating limits obtained for slurries with different flow behavior are compared with Ruschak's [28] visco-capillary model, which is widely used to predict the operating limits of coating processes [29]. Furthermore, electrodes were made from the different slurries and were characterized in terms of microstructure, resistivity and peel strength, and finally, cells were made, and C-rate capability was analyzed to provide a full picture of the impact of mixing procedures on the application case.

2. Materials and Methods

2.1. Mixing Setup

An intensive mixer (EL 1, Maschinenfabrik Gustav Eirich GmbH, Hardheim, Germany) was used to disperse the electrode suspensions and prepare the polymer solutions. In principle, the mixer consists of a pan rotating at a circumferential speed of ω_P and a dispersing tool running at a circumferential speed of ω_w, as shown in Figure 1a; both the tool and the pan rotate clockwise. The dispersion tool has a star-like shape, with pins welded onto the tips—six pins on the top, two on the bottom. To create a mass flow, the

pan conveys the material to a static scraper, which directs the mass towards the dispersing tool, creating an elliptical flow pattern, hence the mass does not fully cover the pan floor. The mixer was used in a horizontal position, at room temperature (22 °C).

Figure 1. (**a**) Schematic drawing of the intensive mixer showing the dispersion tool, the pan and the material; circumferential speed of the dispersing tool (ω_w) and the pan (ω_P); (**b**) solids content (square) and sample volume (circle) during the different mixing procedure steps.

2.2. Slurry Mixing

In a preliminary step, the binder solution was prepared by dissolving CMC (molecular weight M_W = 875 kDa, degree of substitution DS = 0.9, Walocel CRT 30,000 P BA, DDP Specialty Products Germany GmbH & Co. KG, Walsrode, Germany) in deionized water overnight at a concentration of c_{CMC} = 2 wt%. This CMC solution was used to prepare the slurry. Artificial graphite (SCMG-CF-C, Showa Denko Materials (Europe) GmbH, Düsseldorf, Germany) with a volume weighted mean diameter D_{50} of 6.2 μm and a BET surface area of 3.5 m^2 g^{-1} (according to the manufacturer) was used as the main active material and silicon oxide (SiO$_x$; grade H80; D_{50} = 5.5 μm, BET = 8.0 m^2 g^{-1}; Daejoo Electronic Materials Co., Ltd., Siheung, Republic of Korea) was used as a secondary AM for slurry preparation. The mixing weight ratio of both AMs was 9:1 (Gr:SiO$_x$) and the total dry active material content was set to 96.2 wt%. Carbon black (C-NERGY SUPER C45, Imerys Graphite & Carbon, Bodio, Switzerland) was used as conductive additive. CB, CMC and SBR (BM-451; Zeon Europe GmbH, Düsseldorf, Germany) were added in mass according to Table 1. The total solids content of the slurries was set to 60 wt.%.
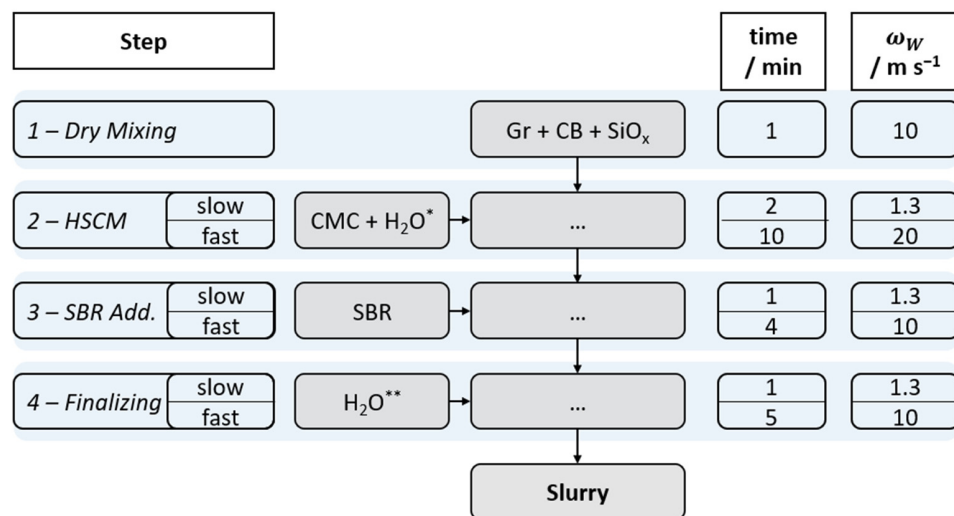
Table 1. Gravimetric composition of the slurry with and without solvent.

Material	Gravimetric Content (NV)/wt%	Gravimetric Content (NV + V)/wt%
Graphite	86.58	51.95
SiO$_x$	9.62	5.77
CB	2.00	1.20
CMC	0.90	0.54
SBR	0.90	0.54
Water	-	40.00

V—volatile; NV—nonvolatile.

The slurry mixing procedure follows the sequences shown in Figure 2. In the first step, the active and conductive materials were mixed dry for one minute at a circumferential tool speed ω_w = 10 m s^{-1}, after which a 2.0 wt% CMC solution was added to the powder. To achieve the desired difference in solids content x_i during high solids content mixing (HSCM) (step 2), a varying amount of water was added to the mixture, resulting in x_i = 60, 63, 66 and 69 wt%, as seen in Figure 1b—the corresponding mixing procedures are labeled

as P_i. In step 3, SBR was added and finally, in step 4, the slurry was finalized by dilution to the desired composition, as shown in Table 1.

Figure 2. Steps of the slurry mixing procedure; steps 2, 3 and 4 each comprise a first period with low and a second period with high stirring speed. * H_2O adjustment to create different solids contents x_i in HSCM step; ** Second H_2O dilution of the slurry to finalize it to the desired TSC.

Due to the variation in water addition in step 2, the mixer's degree of filling varied throughout the procedure; therefore, the occupied sample volume V_{Step} varied, which has to be considered when calculating the specific energy input.

A short and slow mixing sequence with ω_w = 1.3 m s^{-1} was introduced into the procedure to avoid splashing or the formation of dust clouds after the addition of new materials in steps 2, 3 and 4. Following this slow sequence, the actual sequence with the desired fast tool speed started.

In order to shed light on the adsorption and shear-induced degradation of CMC during slurry preparation, a series of aqueous solutions of the CMC used in the slurries, as well as of a low-molecular-weight CMC grade (M_W = 500 kDa, DS = 0.9, TEXTURECEL™ 2000 PA, DDP Specialty Products Germany GmbH & Co. KG, Walsrode, Germany), was prepared and their flow curves were determined using rotational rheometry.

In the second step of the mixing procedure, the stirrer speed was 20 m s^{-1}, corresponding to a high energy input, as will be discussed below. For reference, the slurry S_{Low} was prepared at a significantly lower speed of ω_w = 3 m s^{-1} in this mixing step and the solids content in this step was set to x_i = 60 wt%; the detailed procedure can be seen in Supplementary Figure S1.

2.3. Treatment of Slurry

For further investigation of the binders, the slurry was treated in a centrifuge (Z366, Hermle Labortechnik GmbH, Wehingen, Germany) for 12 h at a relative centrifugal force of RCF = 6300 to separate the solid fraction from the liquid fraction.

2.4. Energy Input

The power consumption P_{el} of the rotor of the dispersing tools was tracked by the machine and integrated over time t, resulting in the energy consumption E of the rotor.

$$E = \int P_{el} dt \qquad (1)$$

Specific energy input E_{sp} was calculated by subtracting idle energy consumption E_{idle} from rotor energy consumption E. This effective energy input E_{eff} was then divided by the sample volume occupied during the mixing step V_{Step} to give E_{sp}.

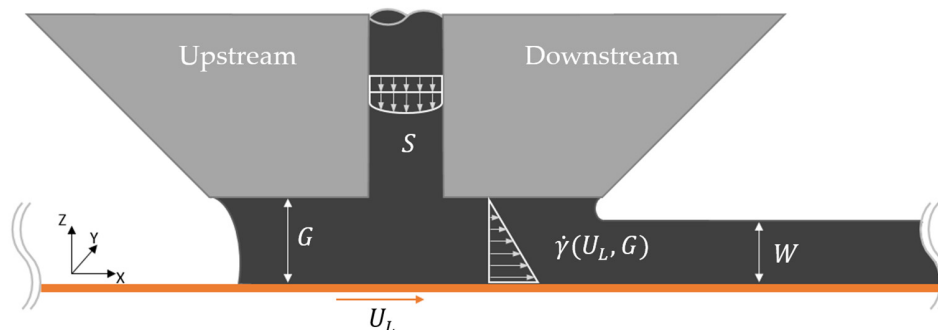$$E_{sp} = \frac{E - E_{idle}}{V_{Step}} = \frac{E_{eff}}{V_{Step}} \tag{2}$$

2.5. Rheology and Coating

Rheological measurements were carried out using a rotational rheometer (MCR 302e, Anton Paar Germany GmbH, Ostfildern, Germany). A plate–plate setup with a diameter of 50 mm and a gap height of 0.3 mm was used as the measurement geometry. The temperature was set to 25 °C.

Shear-rate-controlled measurements were performed using a logarithmic shear rate ramp ranging from $\dot{\gamma} = 0.05$ to 1000 s^{-1} with a measurement duration ranging from 80 s at the lowest shear rate to 2 s at the highest shear rate. For stress-controlled measurements, shear stress τ was increased logarithmically, from 0.01 to 1000 Pa with a measurement time of 18 s for each stress value.

When analyzing the coating experiments, the shear rate within the coating layer was calculated as the ratio of the line speed U_L and the slot-die gap, i.e., the distance between the slot-die lips and the substrate G, see Figure 3.

$$\dot{\gamma} = \frac{U_L}{G} \tag{3}$$

Figure 3. Schematic drawing of a slot-die, including flow pattern within the coating bead.

The dynamic viscosity η corresponding to this shear rate was obtained by interpolating the experimental viscosity vs. shear rate data.

In order to establish the relationship between surface tension σ, dynamic viscosity η and line speed U_L, the dimensionless capillary number Ca was calculated as follows [29,30].

$$Ca = \frac{\eta \cdot U_L}{\sigma} \tag{4}$$

The surface tension of the slurry was set equal to that of pure water at 22 °C, $\sigma = 72.3 \text{ mN m}^{-1}$ [31], which was considered a fair approximation for this hardly accessible quantity since no surface-active ingredients were added to prepare the slurry.

The viscosity data used to calculate Ca were determined at 25 °C; since slot-die coating was performed at 22 °C, this results in a small systematic error. Since the temperature dependence of slurry viscosity is essentially determined by that of water, as the main ingredient of the slurries disperse phase [32], we can estimate this error to be smaller than 7%.

The dynamic gap G^* was calculated as the ratio of the slot-die gap G and the height of the wet film W, see Figure 3. While G is given by the dimensions and setup of the coater

itself, W was calculated from electrode loading, slurry TSC and slurry density, resulting in $W = 87.6$ μm.

$$G^* = \frac{G}{W} \qquad (5)$$

2.6. Coating Experiment

The coating trials were carried out using a roll-to-roll coater manufactured by Mathis AG (Niederhasli, Switzerland). The slot-die was installed with a 300 μm thick shim sheet S and with a slot width of 50 mm. The slurry was fed by a progressing cavity pump. Before the trials, the coater pump was calibrated at the highest stable G^* for each speed of the test run to ensure a constant capacity loading of 3.3 mAh cm^{-2} at each speed. This was performed by coating, drying and weighing cut coins at line speeds from 2 to 10 m min^{-1}, varying in steps of 2 m min^{-1}. The experiments were carried out in a dry room (dew point < −45 °C) at 22 °C.

Two coating defects, air entrainment and widening of the coating, were monitored visually as stability criteria. Here, the upper stability limit (USL) describes the highest values of G^* where no air entrainment was observed and the lower stability limit (LSL)—the lowest value of G^* where no increase in coating width was measured. Air entrainment as a coating defect after exceeding the USL is shown in Figure 4a. Conversely, the widening of the coating after exceeding the LSL was measured by the coater's camera measurement system. Within the stability limits, the coating was uniform and showed no defects, as shown in Figure 4b.

(**a**)   (**b**)

Figure 4. Inline photographs of the roll-to-roll coating experiments, web's direction from bottom to top; (**a**) coating outside stable operating window with visible air entrainment; (**b**) coating within the stable operating window.

For the model-based estimation of the upper stability limit, the visco-capillary model (VCM) by Ruschak was utilized and the critical capillary number was calculated with a numerical prefactor of 0.65 [28,29].

$$Ca_R = 0.65 \left(\frac{2}{G-1} \right)^{\frac{3}{2}} \qquad (6)$$

2.7. Manufacturing of Electrodes

Slurries were degassed at 100 mbar for two minutes. Electrodes were cast using a porous vacuum table (510XL, Erichsen GmbH & Co. KG, Hemer, Germany) and a fixed film applicator frame (BYK-Gardner GmbH, Geretsried, Germany) in the range of 120 to 140 μm via doctor blade coating. Depending on slurry viscosity, the gap height was selected to produce electrodes with a loading of 3.3 mAh cm^2 at 7.9 mg cm^{-2}. Positive electrodes with a loading of 3.0 mAh cm^{-2}, a mass loading of 16 mg cm^{-2} and a compressed electrode thickness of roughly 49 μm were used to construct full pouch cells, containing 94.5 wt% NCM 811 as AM.

Dried table-coated negative electrodes were compressed using a laboratory calender (Ingecal SAS, Chassieu, France) operating at 0.8 kN mm^{-1} using 70 mm wide electrode strips without heating. The electrodes were compressed to an average density of 1.2 g

cm^{-3}, resulting in an electrode thickness of roughly 66 μm. Negative electrodes originating from x_i are labeled as A_i.

2.8. Morphology

Cross-sectional images of the electrodes were taken using a scanning electron microscope (SEM; MIRA3, Tescan Orsay Holding a.s., Brno, Czech Republic). Electrode coins were stamped with a diameter of 15 mm and cut in half. The straight-cut edge was then treated using an ion milling system (IM4000Plus, Hitachi High-Tech Europe GmbH, Krefeld, Germany) and this treated cross-section was then examined.

2.9. Resistivity Measurement

The resistivity of the electrodes was measured using an electrode resistance measuring system (RM2610, Hioki E.E. Corporation, Nagano, Japan). The system presses a 46-pin probe head against the surface of the electrode and measures two resistances: volume resistivity ρ_V in units of Ω cm, representing the resistivity of the electrode layer, and interface resistance ρ_I in units of Ω cm^2, representing the resistivity of the interface between the coating and the substrate [33,34].

Assuming that electron flow in the electrode is perpendicular to the current collector surface, the specific contact resistance ρ_{CN} is given by the product of volume resistivity ρ_V and electrode thickness h [35].

$$\rho_{CN} = \rho_V \cdot h \tag{7}$$

2.10. Peel Test

Peel strength was measured using a zwickiLine Zo.5 (ZwickRoell GmbH & Co. KG, Ulm, Germany) and a 90° peel test setup. The electrodes were cut into 30 mm wide strips with a total substrate length of 200 mm and a coating length of 120 mm. After calendering, the electrode samples were attached to the setup with double-sided adhesive tape (tesa 05696, Tesa SE, Norderstedt, Germany) and the machine measured the force required to peel the substrate from the coating at a speed of 5 mm/s. Peel strength F_{Peel} was calculated by dividing the measured force F_{total} by the width of the sample W_{Sample}.

$$F_{Peel} = \frac{F_{total}}{W_{Sample}} \tag{8}$$

2.11. Cell Manufacturing

Pouch cells with positive electrode dimensions of 25 mm × 40 mm were built using two single-sided negative electrodes and one double-sided positive electrode. The cells were filled with 0.4 mL of LiPF$_6$ electrolyte (carbonate solvent mixture and additive, Soulbrain, Northville Township, MI, USA). A ceramic separator (Enpass D22AEGK, SK innovation Co., Ltd., Seoul, Republic of Korea) with a thickness of 21 μm was used in this process. Cell building was performed in a dry room (dew point < −45 °C) and electrolyte filling was performed in an argon-filled glovebox atmosphere with less than 0.1 ppm O$_2$ and 0.1 ppm H$_2$O. The pouches were evacuated and sealed in this glovebox. The cells balanced at a positive to negative ratio of 1.1 and a slightly larger negative electrode dimensions (27 mm × 42 mm) than the positive electrode surface area.

2.12. Electrochemical Measurements

Cell formation and later a C-rate test were carried out using a CTS (Basytec GmbH, Asselfingen, Germany) at 25 °C with a cut-off potential of 2.8 and 4.2 V. A set of four cells per electrode variation was investigated. The cells were pressurized by using plastic plates and clamps.
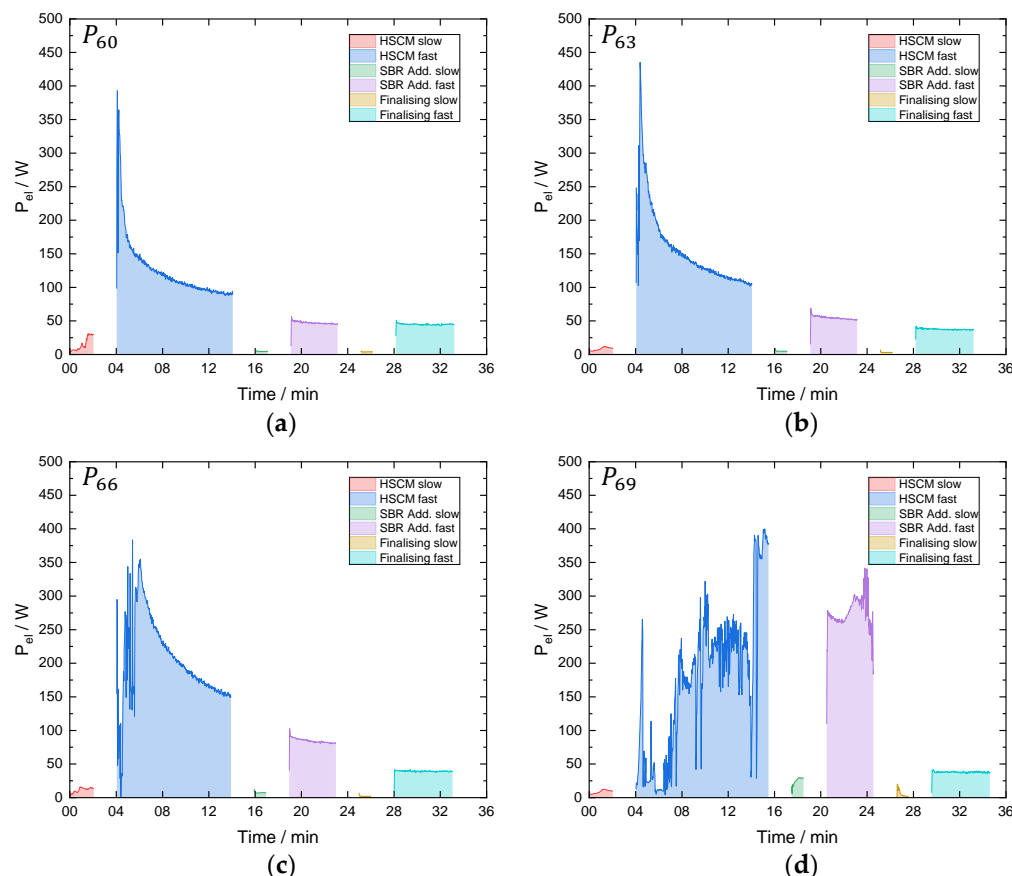
During formation, the cells were charged by applying a CCCV regime to them with C-rates ranging from 0.1 to 0.33 C. The discharge step occurred with the same C-rates as the charging step, following a CC regime. The C-rate tests can be divided into two segments,

discharge C-rate and charge C-rate. Both segments started with 2 cycles at 0.33 C, followed by 10 steps consisting of 3 constant current cycles with increasing C-rate ranging from 0.5 C to 5 C. At the end of the test, two check-up cycles at 0.3 C were performed.

3. Results and Discussion

3.1. Energy Input

Variation in the mixing procedures here essentially refers to varying the solids content x_i during the HSCM step. This variation resulted in different energy inputs within the process variations P_i. Figure 5 shows the total power consumption of the mixer for steps 2 to 4 of the procedure; these are the steps where the solvent was included.

Figure 5. Total rotor power consumption for the four variations of the mixing procedure P_i; high solids content mixing (HSCM) occurred at x_i equal to 60 (**a**), 63 (**b**), 66 (**c**) and 69 (**d**) wt% solids content; legends refer to mixing steps 2, 3 and 4, as described in Figure 2: high solids content mixing (HSCM), addition of SBR, and finalization by water addition to reach the target TSC 60 wt%.

During the processing of P_{60}, power consumption follows a typical profile for mixing suspensions [36], best seen in the fast HSCM step. On starting, the bulk mass transforms into a plastic mass, resulting in the peak of rotor power. As the wetting and dispersion of the particles continue, the plastic mass changes to a viscous suspension, while power consumption decreases and asymptotically approaches a constant level. It can be seen that as x_i increases, total power consumption changes drastically. While P_{63} and P_{66} are comparable to the power consumption pattern of P_{60}, procedure P_{69} undergoes a drastic change in power consumption, and thus in energy input. Here, the HSCM step does not produce a fluid suspension, but rather a plastic mass. This mass moves through the mixer and sporadically touches the rotor, resulting in a constant formation of power peaks rather than a steady mass flow that eventually approaches a steady power level. For this reason, the duration of the HSCM step in procedure P_{69} was slightly increased by 2 min to account for the initial period of no mixing.

Table 2 shows the specific energy inputs as calculated using Equation (1). It can be seen that an increase in x_i leads to a higher energy input. Comparing the two most extreme variations, P_{60} and P_{69}, P_{69} differs from P_{60} by a factor of about 3; therefore, a stronger deagglomeration might be expected with increasing x_i. It is noticeable that the largest contribution to energy input comes from the HSCM step, but in P_{69}, the SBR addition step also contributes significantly. Comparing P_{60} and P_{69}, the specific energy input of this step differs by a factor of about 11. The "Finalization fast" step shows similar energy inputs for all slurries (see Figure 5), with an average value of 2.5 Wh dm^3, which could lead to the false assumption that all slurries have similar flow behavior. As for the low-energy reference, P_{Low} showed an energy input of roughly one-third of P_{60}; detailed consumption can be seen in Figure S1.
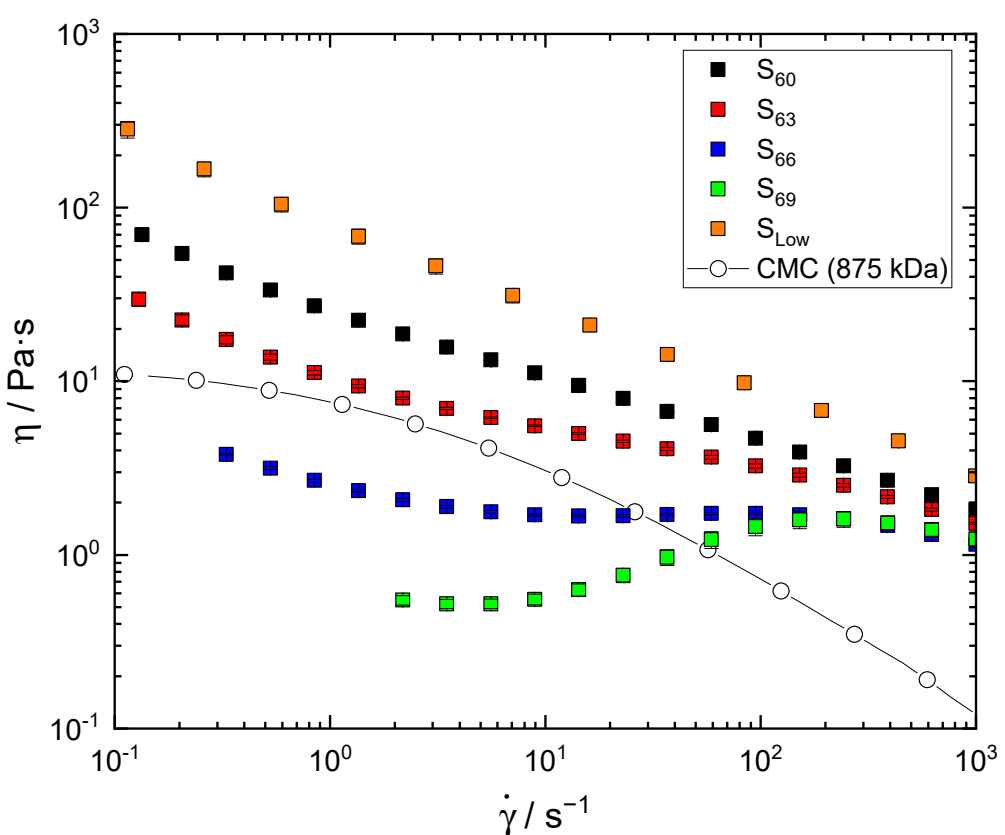
Table 2. Specific energy input for all mixing procedure variations P_i originating from the change in x_i; total amount of specific energy input and specific energy input at step 3, the dispersion of SBR.

Specific Energy Input	P_{60}	P_{63}	P_{66}	P_{69}	P_{Low}
E_{sp}/Wh dm^{-3}	29.1	45.0	59.0	85.9	11.5
E_{sp} of step 3 (SBR)/Wh dm^{-3}	3.0	4.1	7.7	31.9	0.6

3.2. Flow Behavior

For a more detailed picture of flow behavior, the flow curves of all four slurries S_{60} to S_{69} as well as S_{Low} and the CMC (M$_w$ = 875 kDa) solution with a concentration of 13.5 g L^{-1}, corresponding to the nominal CMC concentration in the aqueous phase of the slurry, are shown in Figure 6. All slurries have the same composition and TSC, but their flow behavior is very different. Overall, with increasing solids content x_i during HSCM, the low shear viscosity of the slurries decreases up to two orders of magnitude, despite their identical composition. According to Stokes' law, it is to be expected that slurries with lower low shear viscosity will sediment faster and will therefore be less stable. In small batches, this may not be a problem, but on an industrial scale, this could lead to stability problems when using the slurry for a long period of time without stirring.

The low energy input sample S_{Low} shows the highest viscosity values and demonstrates uniform, power-law-type shear thinning behavior. Slurries S_{60} and S_{63} also show monotonic shear thinning behavior, but their absolute viscosity values are lower and the degree of shear thinning is less pronounced than those of S_{Low}. Absolute viscosity values further decrease with increasing x_i or energy input during the HSCM mixing step. Furthermore, slurries S_{66} and S_{69} do not show strict shear thinning behavior. Slurry S_{66} exhibits weak shear thinning behavior only at low shear rates, approaches a plateau between roughly 10 and 200 s^{-1} and finally the viscosity decreases again at higher shear rates. Slurry S_{69} shows shear thickening behavior between 10 and 200 s^{-1}, followed by a shear thinning regime at higher $\dot{\gamma}$.
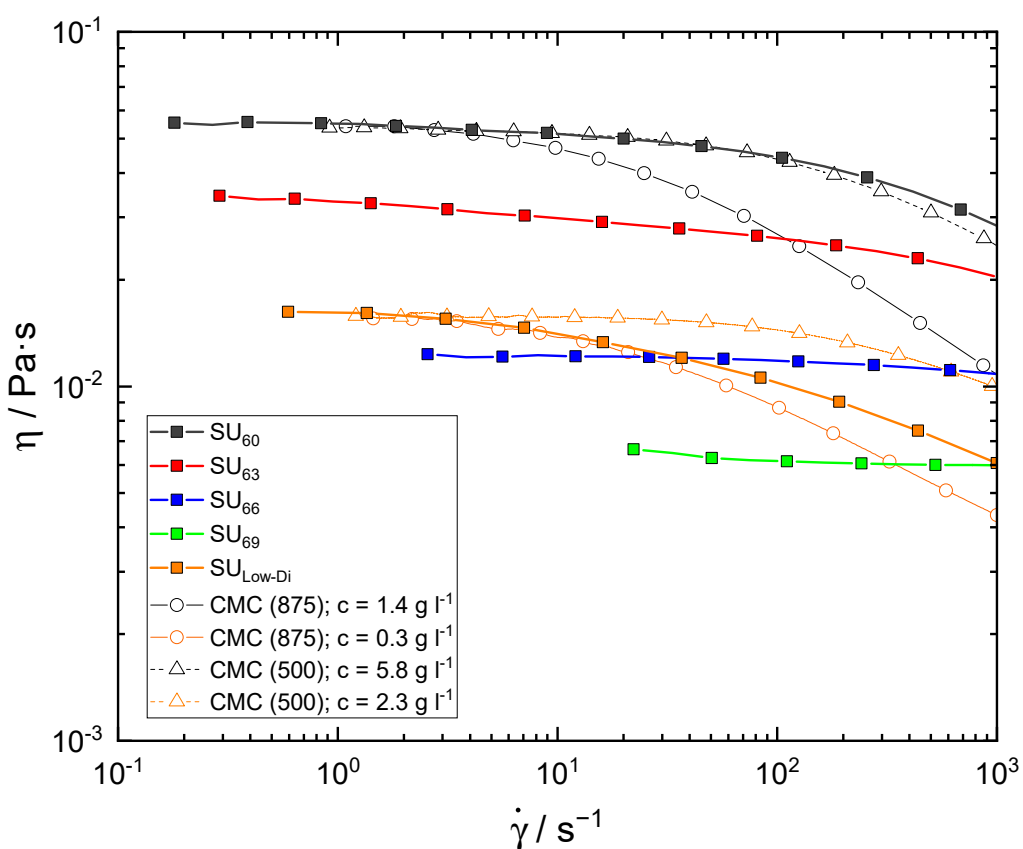
Figure 6. Viscosity as a function of shear rate for slurries with TSC = 60 wt%, but mixed at different solids content during HSCM; x_i = 60 (black), 63 (red), 66 (blue), 69 wt% (green) and low energy input reference slurry x_{Low} (orange). The flow curve for a CMC solution (open symbols) with the same molecular weight Mw = 875 kDa as that used for slurry preparation and polymer concentration (13.5 g L^{-1}) corresponding to that in the disperse phase of the slurry is shown for comparison.

These drastic differences in flow behavior for slurries of identical composition are direct evidence of different particle interactions and hence different microstructures due to different slurry treatment, i.e., different energy input during mixing. One reason for such changes in flow behavior could be a difference in particle deagglomeration and the existence of particle clusters trapping a substantial fraction of the solvent and thus leading to a higher effective particle volume fraction at low energy input. However, all slurries appeared well dispersed, and SEM images of corresponding dry samples did not show evidence of remaining particle clusters. A potential mechanical destruction of the solids fraction and a corresponding change in particle size distribution is not expected to have affected slurry viscosity since the overall particle loading of about 40 vol% is too low [32] and SEM images of corresponding dry samples do not provide experimental evidence for that. Finally, the flow behavior of suspensions strongly depends on the colloidal interactions among the suspended particles, as well as on solvent rheology [32]. For the slurries investigated here, these phenomena are closely related to the adsorption of CMC on the solid particle surfaces [37] and the mechanical degradation of CMC [38,39] during slurry preparation. The relevance of CMC adsorption and presumably also degradation already shows up when comparing the low shear viscosity of slurries S_{66} and S_{69} to that of the CMC solution representing the disperse phase of these slurries. The low absolute viscosity values of slurries S_{66} and S_{69} can only be rationalized taking into account these adsorption and degradation phenomena, as will be discussed in more detail below.

The pronounced shear thickening of sample S_{69} is attributed to the formation of hydrodynamic clusters. Such clusters can only form when none or only weak, short-range repulsive interactions among particles are present [32]; this also results in low viscosity

at low shear rates, as observed for S_{69}. In this case, the steric repulsion inferred from an adsorbed CMC layer seems to just compensate for the always present van der Waals attraction. The latter, on the other hand, seems to dominate in the shear thinning samples S_{60}, S_{63} and particularly S_{Low}. Obviously, energy input during the HSCM mixing step has a significant impact on CMC adorption. Additionally, the mechanical degradation of CMC has to be considered, since it affects both the viscosity of the solvent and the strength and range of the steric repulsion provided by the CMC adsorbed on the active particle surface. The reference sample S_{Low} prepared in a different manner and at a low energy input exhibits the highest viscosity level and the strongest degree of shear thinning, clearly indicating that attractive particle interactions dominate in this slurry.

Figure 7 shows the flow curves for the supernatants (SU_i) obtained from the centrifugation of the slurries S_i. It should be noted that the supernatant of slurry S_{Low} was diluted with deionized water at a ratio 1:26 (supernatant/water) due to its high viscosity not allowing for the determination of zero shear viscosity; therefore, the dilution is labeled as S_{Low-Di}. The viscosity functions of these supernatants are essentially determined by the concentrations and molecular weights of the dissolved CMC; the contribution of suspended SBR particles or residual active material is negligible. The absolute viscosity values differ by about an order of magnitude, indicating that the degree of CMC removed from the disperse phase via adsorption on the active particles is strongly affected by the slurry preparation procedure. The sample with the highest energy input during the HSCM mixing step has the lowest disperse-phase viscosity, indicating that a larger fraction of CMC is adsorbed on the particles in this case, consistent with the flow behavior of the slurry itself. Moreover, supernatants SU_{60}, SU_{63} and the diluted supernatant SU_{Low-Di} exhibit shear thinning behavior, whereas samples SU_{66} and SU_{69} show Newtonian flow behavior. This provides further insight into the mechanically induced adsorption and degradation of CMC in these slurries. Highly diluted CMC solutions show Newtonian flow behavior and solutions with different molecular weights and concentrations may exhibit the same absolute viscosity value. More highly concentrated solutions, however, are shear thinning and the absolute value of zero shear viscosity and the shape of the flow curve are a unique signature of a solution with a certain molecular weight and CMC concentration [40]. Figure 7 includes the flow curves of CMC solutions with M_w = 875 kDa and M_w = 500 kDa, matching the zero shear viscosity of supernatants SU_{60} and SU_{Low-Di}, respectively. Obviously, a higher concentration is required for the solution of CMC with lower molecular weight to achieve the same zero shear viscosity as for the solution of CMC with higher molecular weight. Moreover, shear thinning is significantly more pronounced for the solution of CMC with higher molecular weight. The CMC solution with M_w = 875 kDa and c_{CMC} = 0.3 g L^{-1} almost matches the flow curve of the diluted supernatant SU_{Low-Di}. Its slightly more pronounced shear thinning indicates that some mechanical degradation also occured in this case, but for the sake of simplicity, we neglected that. Under this assumption, the difference between this concentration and the input concentration of 13.5 g L^{-1} (see Table 1 and Figure 6) directly denotes the amount of CMC adsorbed on the particles. As exemplarily demonstrated using the solution with M_w = 500 kDa and c_{CMC} = 2.3 g L^{-1}, solutions of CMC with other molecular weights yield different shear thinning behaviors even if their zero shear viscosities matches. For supernatant SU_{60}, the situation is different; in this case, the CMC solution with M_w = 875 kDa matching its zero shear viscosity exhibits much more pronounced shear thinning than the supernatant. This is direct evidence that the CMC molecules experienced degradation during the mixing process. In contrast, the CMC solution with M_w = 500 kDa and c_{CMC} = 5.8 g L^{-1} resembles the absolute values and shape of the flow curve in the whole investigated shear rate range well. We conclude that the CMC experienced mechanical degradation roughly to this average molecular weight and, again, we can calculate the amount of the adsorbed CMC as the difference between the concentration of this solution and the CMC input concentration.

Figure 7. Viscosity as a function of shear rate for supernatants (SU_i) of the slurries that were mixed at different solids contents during HSCM; $x_i = 60$ (black), 63 (red), 66 (blue), 69 wt% (green) and low energy input reference slurry $x_i = 60$ (orange); CMC solution (875 kDa; circle) with 1.4 (black) and 0.3 (orange) g L^{-1} and C C solution (500 kDa; triangle) with 2.3 (black) and 5.8 (orange) g L^{-1}.

Finally, we conclude that for S_{60}, almost 57 wt% of added CMC adsorbed on the surface of the active particles and for S_{Low}, about 42 wt% was adsorbed, taking into account supernatant dilution (see Supplementary). The supernatants SU_{66} and SU_{69} show rather Newtonian flow behavior and it is not possible to assign the measured viscosity unambiguously to a certain M_w and concentration of the dissolved CMC. Assuming that with increasing energy input, no further degradation of molecular weight takes place, we can determine the CMC concentration in the supernatant from the η_0 vs. c_{CMC} data for a series of CMC solutions with $M_w = 500$ kDa shown in the Supplementary Information (Figure S2). Under this constraint, it turns out that the fraction of adsorbed CMC increases with increasing energy input and for slurry S_{69}, almost all CMC is adsorbed on the particles. This is consistent with the observed changes in the flow curves of the corresponding slurries, which can be rationalized assuming a stronger steric repulsion for S_{69} finally balancing the attractive van der Waals force. On the other hand, if we assume a pronounced further degradation of CMC chains with increasing energy input, then the measured supernatant viscosity curves would imply that a smaller fraction of shorter CMC chains was adsorbed onto the active material particles, which contradicts the observed decrease in slurry viscosity. This supports the assumption that no further mechanical CMC degradation took place in the slurries prepared at higher energy input than S_{60}.
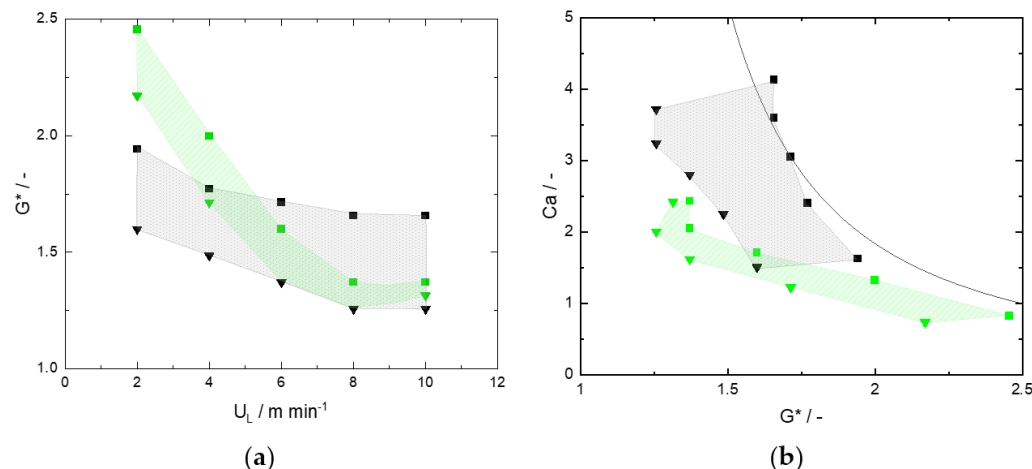
A similar effect of mechanical energy input on CMC adsorption was recently published by Park et al. [41] However, the group did not consider mechanical degradation as they already used a low molecular weight CMC.

Weber at al. [42] investigated the impact of dry mixing CB and Gr as a preliminary step before mixing it with the solvent in an extruder. Varying the tip speed during dry mixing resulted in different flow behavior in the final slurries, ranging from a rather

monotonous shear thinning behavior to a discrete plateau. Perhaps the pretreatment of the powder resulted in different surface availability or different energy input during extrusion, resulting in a varying degree of polymer adsorption and degradation, finally changing particle-particle interactions and thus flow behavior as discussed above.

3.3. Coating

To investigate the influence of the slurries' flow behavior on coating, experiments were carried out with slurries S_{60} and S_{69}, as they showed the greatest differences in flow behavior. The two slurries were coated at different line speeds; the maximum and minimum G were determined for the upper and lower stability limits. The results are shown in Figure 8a, which shows the dynamic gap G^* of both stability limits as a function of line speed U_L. For slurry S_{60}, the USL slightly decreases with increasing line speed, ranging from a dynamic gap of 1.9 to 1.7. The difference ΔG^* between USL and LSL increases with increasing U_L, from 2 to 10 m min^{-1}, roughly to $\Delta G^* = 0.3$. Slurry S_{69} shows a more radical change in its stability limits. Its initially high USL of roughly $G^* = 2.5$ at 2 m min^{-1} decreases to $G^* = 1.4$ at 10 m min^{-1}. The corresponding LSL decreases in a similar way; however, at 10 m min^1, the lower limit closes up to the upper limit with $G^* = 1.3$. Whereas S_{60} demonstrates a broad corridor of stable operation limits in this coater setup, S_{69} displays a rather narrow window of stable operating parameters. Such a narrow window makes the coating of S_{69} difficult, especially at higher speeds.

(a) (b)

Figure 8. Stability map for slot-die coating of slurries S_{60} (black) and S_{69} (green); USL—square symbol; LSL—triangle symbol; (**a**) dynamic gap as a function of line speed; (**b**) capillary number as a function of dynamic gap, including the VCM of Ruschak 1976 [28] (Equation (6), straight line).
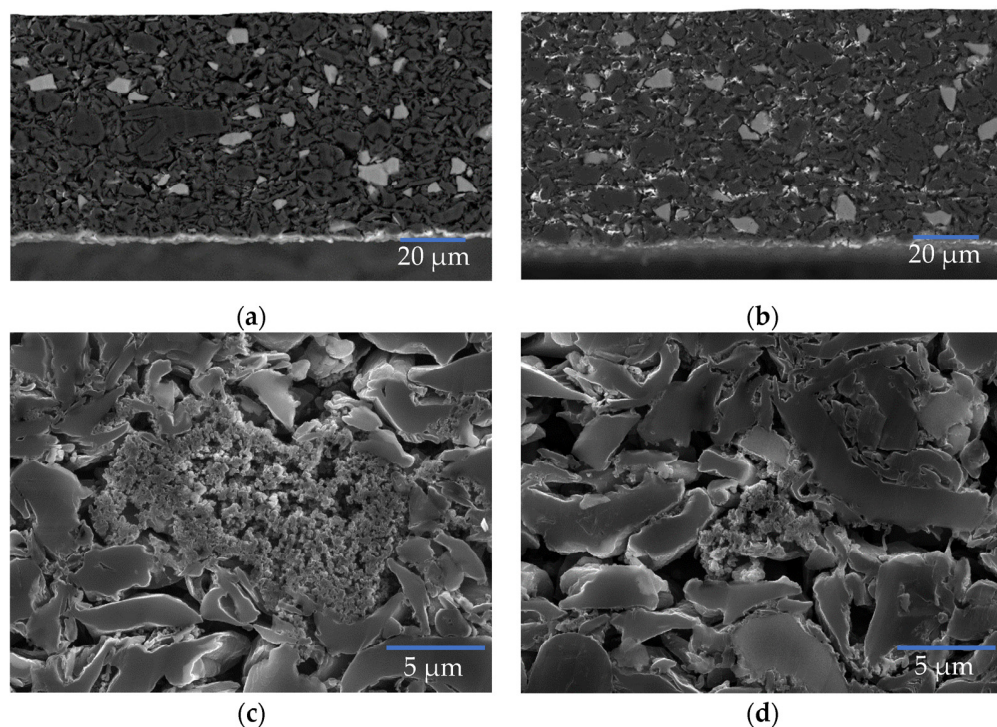
In order to compare these results with the visco-capillary model of Ruschak [28], a stability map was plotted in the Ca -G^* plane (Equations (4) and (5)), as shown in Figure 8b. It should be noted that the VCM of Ruschak [28] was developed on Newtonian fluids. Focusing on the upper limit, at 2 m min^{-1}, slurry S_{60} could be coated with $G^* = 1.9$ at $Ca = 1.6$ and at 10 m min^{-1}, a stable coating was achieved with $G^* = 1.7$ at $Ca = 4.1$. This USL border is close to that predicted by Ruschak; however, the decay of Ca with increasing G^* is more pronounced. In contrast, slurry S_{69} maintained a USL at 2 m min^{-1} with $G^* = 2.5$ at $Ca = 0.8$ and at 10 m min^{-1} with $G^* = 1.4$ at $Ca = 2.4$. Here, only for very high $G^* = 2.5$ is the VCM prediction approached. This comparison indicates that the coating behavior of monotonically shear thinning slurries such as S_{60} can be predicted with respect to line speed and gap height settings, whereas more complex slurries such as the shear thickening S_{69} are not represented by the model.

Whenever the upper stability border was crossed, air entrainment was observed, which is related to the failure of the upstream meniscus. In the case of S_{69}, this might be due to its overall lower viscosity. The resulting capillary number is significantly lower than

that of S_{60}, indicating that the viscous forces are less pronounced. Ultimately, this leads to a closing-up of the upstream meniscus towards the coating bead and the entrainment of air occurring at a lower G^* than it would with S_{60}. Due to the narrow stability window of S_{69}, coating at higher speeds might be very challenging; here, the installation of a vacuum box upstream could be helpful.
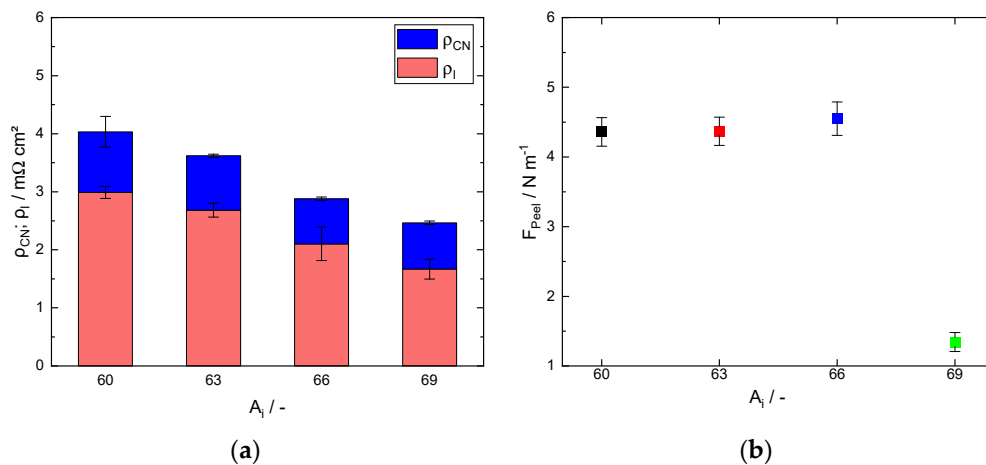
3.4. Electrode Microstructure

Table-coated electrodes originating from the four slurries were characterized with a loading of 3.3 mAh cm^{-2} and an average compressed density of 1.2 g cm^{-3}. Electrodes A_{60} to A_{69} were analyzed using a scanning electron microscope equipped with a backscattered electron detector (BSE). A_{60} and A_{69} are shown in Figure 9. Due to the differences in E_{sp}, an impact on particle deagglomeration, especially of carbon black, might be expected. Nevertheless, the overall active material distribution is equally homogeneous. However, A_{60} electrodes show more and larger CB aggregates than A_{69}, as shown in Figure 9c,d. Since the total energy input varied by a factor of about three, this seems plausible.

Figure 9. SEM cross-section of investigated compressed electrodes A_{60} (**a**,**c**) and A_{69} (**b**,**d**).

Following up on the effect of dispersed CB, total electrode resistivity, divided into ρ_I and ρ_{CN} (Equation (7)), is shown in Figure 10a. Resistivity decreases with increasing energy input from a total of about 4 ± 0.4 to 2.5 ± 0.2 mΩ cm^2. This trend can be observed in both parts of the electrode: the resistivity of the coating and the resistance of the interface. However, the most noticeable difference in this series is interfacial resistance: $\rho_{I;A_{60}} = 3.0 \pm 0.1$ and $\rho_{I;A_{69}} = 1.7 \pm 0.2$ mΩ cm^2. A possible reason for this decrease in interfacial resistivity could be that with increasing energy input, a greater fraction of CMC is adsorbed on the active material particles, as discussed in the rheology section above. Therefore, less CMC is available at the coating/substrate interface, thus lowering interfacial resistivity. On the other hand, the resistivity of the coating layer itself does not vary much: $\rho_{CN;A_{60}} = 1 \pm 0.27$ and $\rho_{CN;A_{69}} = 0.8 \pm 0.03$ mΩ cm^2. Although the size of the CB agglomerates decreases with increasing x_i, this seems to have little effect on the resistivity of the coating layer in these graphite-based electrodes.
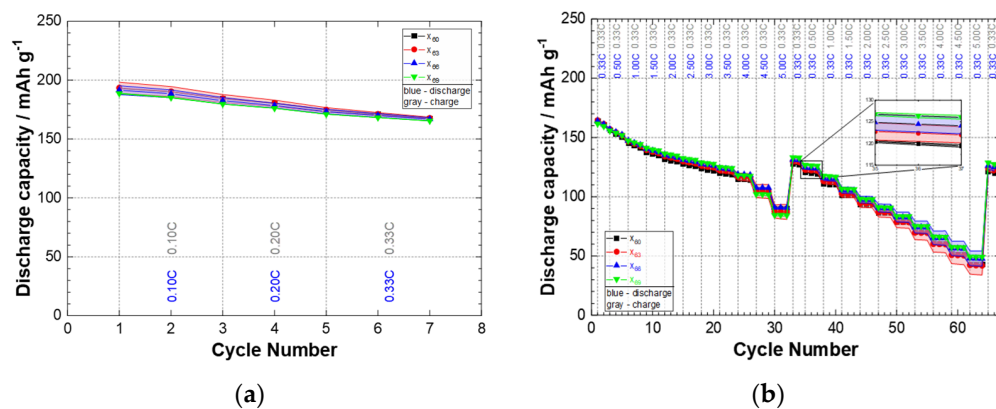
Figure 10. (**a**) Resistivity of compressed electrodes A_{60} to A_{69} determined using an electrode resistance measurement system; (**b**) peel strength of compressed electrodes A_{60} to A_{69}.

　　　Adhesion between the electrode and the current collector was characterized by a 90° peel test; corresponding data for A_{60} to A_{69} are shown in Figure 10b. While electrodes A_{60} to A_{66} show a similar peel strength of about 4.4 N m^1, sample A_{69} shows a drop in adhesion to a peel strength value of about 1.3 N m^1. Such a low adhesion as that of A_{69} might be challenging for automated processes within cell assembly due to delamination of the coating. Adhesion is mainly provided by the added SBR [43] and the high energy input in step 2 (HSCM) of the procedure apparently has a significant effect on SBR distribution, with a significantly lower SBR fraction at the current collector interface for A_{69} which may be due to a shear-induced agglomeration of SBR particles.

3.5. Cell

　　　Table-coated electrodes A_{60} to A_{69} were used to build small-format pouch cells. Figure 11 shows the discharge capacity of the formation on the left and the discharge capacity of the C-rate test on the right. Four cells per A_i were measured. Within the formation, all cells run at very similar capacities, but cells originating from higher x_i start to show less capacity, fading towards the seventh cycle. When discharging (cycles 1 to 32) at different C-rates, A_{69} runs at the highest capacity, excluding 4.5 and 5.0 C, which is dominated by ionic limitations of the positive electrode. Charging at different C-rates (cycle 33 to 64) also shows that A_{69} appears to outperform the other cells, indicating differences in microstructure. In the check-up, represented by the last two cycles of the C-rate test (cycle 65 and 66), A_{69} again shows the highest capacity.

Figure 11. Cycling data of investigated full pouch cells: (**a**) formation; (**b**) C-rate test.

Taking a closer look at the charge segment of the test, capacity follows a trend, with A_{69} having the highest values and A_{60} running at the lowest, see cycle 36. This correlates well with the resistance measurements in Figure 10, where A_{69} has the lowest resistance, which ultimately results in higher charge capabilities, due to a longer charging time before reaching cut-off criteria. As can be seen in the charge step 3C (cycle 51), A_{69} runs at 83.5 ± 0.4 mAh g^{-1} and A_{60} at 78 ± 0.7 mAh g^{-1}, showing a difference of roughly 6%. These data show that although the same materials and compositions were used in all four slurries, cell performance can be increased simply by mixing the slurry with a variation in x_i—solids content during kneading—thus changing the energy input of the mixing procedure.

4. Conclusions

Anode slurries containing graphite and silicon oxide as active materials, carbon black as the conductivity agent, and CMC and SBR as binders, with the same composition and total solids contents, were prepared at different energy inputs during slurry preparation and their impact on slurry rheology, coating behavior, mechanical and electrical properties of the resulting dry electrodes, and the electrochemical performance of cells made from these negative electrodes was investigated. Slurries were prepared using an intensive mixer and energy input varied over a wide range by adjusting the solids content during the mixing step, wherein water and a CMC solution were added to the dry mixture of graphite, SiO$_x$ and CB. This energy input during slurry preparation affects the deagglomeration of CB to some extent, but more importantly, it controls the mechanical degradation of CMC and its adsorption on the surface of the active material particles. The fraction of adsorbed CMC on the particles increases with increasing energy input and the corresponding increase in steric repulsion among the suspended particles leads to a drastic change in slurry rheology. The low shear viscosity and the degree of shear thinning decreases with increasing energy input, and at the highest energy level, steric repulsion balances the van der Waals attraction, resulting in an almost Newtonian flow behavior at low shear rates and pronounced shear thickening at high shear rates. The reduced viscosity at high energy inputs results in a narrower stability window during slot-die coating. The variation in CMC adsorption is also evident in the contact resistivity between the electrode layer and the current collector, which decreases as more CMC is adsorbed on the active material particles. Energy input also appears to have an effect on the distribution or agglomeration of SBR, as shown by a drastic drop in the peel strength of electrodes at the highest level of mixing energy input. Finally, the pouch cells built with the electrodes made from the differently prepared slurries all show good electrochemical performance. The cell based on the slurry prepared with the highest energy input exhibits a slightly higher charge capability compared to the cell made from the slurry prepared with the lowest energy input. The later slurry, however, exhibited a broader slot-die coating window, thus promising a more robust processing behavior.

All in all, we have shown that the mixing protocol and hence the energy input during slurry preparation can have a significant impact on the microstructure and flow behavior of slurries, which is directly reflected in their coating behavior, but also propagates to the mechanical and electrical properties of dry electrode layers and finally manifests itself in the electrochemical performance of the corresponding cells. Therefore, we conclude that a carefully tuned mixing procedure can exploit the best electrochemical potential without sacrificing process-relevant properties such as peel strength or flow behavior. Future investigations into tailored mixing strategies should include other active material compositions such as silicon-rich powder mixtures or positive electrode materials such as LFP or high nickel NMC, as well as alternative binder systems such as polyacrylic acid or sodium alginate.

References

1. Liu, Y.; Zhang, R.; Wang, J.; Wang, Y. Current and future lithium-ion battery manufacturing. *iScience* **2021**, *24*, 102332. [CrossRef] [PubMed]

2. Bauer, W.; Nötzel, D.; Wenzel, V.; Nirschl, H. Influence of dry mixing and distribution of conductive additives in cathodes for lithium ion batteries. *J. Power Sourc.* **2015**, *288*, 359–367. [CrossRef]

3. Bitsch, B.; Willenbacher, N.; Wenzel, V.; Schmelzle, S.; Nirschl, H. Einflüsse der mechanischen Verfahrenstechnik auf die Herstellung von Elektroden für Lithium-Ionen-Batterien. *Chem. Ing. Tech.* **2015**, *87*, 1–10. [CrossRef]

4. Liu, D.; Chen, L.-C.; Liu, T.-J.; Fan, T.; Tsou, E.-Y.; Tiu, C. An Effective Mixing for Lithium Ion Battery Slurries. *Adv. Chem. Eng. Sci.* **2014**, *4*, 515–528. [CrossRef]

5. Nakajima, H.; Kitahara, T.; Higashinaka, Y.; Nagata, Y. Effect of Electrode Mixing Conditions on the Performance of Lithium-Ion Batteries Analyzed by Fast Fourier Transform Electrochemical Impedance Spectroscopy. *ECS Trans.* **2015**, *64*, 87–95. [CrossRef]

6. Wang, M.; Dang, D.; Meyer, A.; Arsenault, R.; Cheng, Y.-T. Effects of the Mixing Sequence on Making Lithium Ion Battery Electrodes. *J. Electrochem. Soc.* **2020**, *167*, 100518. [CrossRef]

7. Kwade, A.; Haselrieder, W.; Leithoff, R.; Modlinger, A.; Dietrich, F.; Droeder, K. Current status and challenges for auto-motive battery production technologies. *Nat. Energy* **2018**, *3*, 290–300. [CrossRef]

8. Hawley, W.B.; Li, J. Electrode manufacturing for lithium-ion batteries—Analysis of current and next generation processing. *J. Energy Storage* **2019**, *25*, 100862. [CrossRef]

9. Nitta, N.; Wu, F.; Lee, J.T.; Yushin, G. Li-ion battery materials: Present and future. *Mater. Today* **2015**, *18*, 252–264. [CrossRef]

10. Chartrel, T.; Ndour, M.; Bonnet, V.; Cavalaglio, S.; Aymard, L.; Dolhem, F.; Monconduit, L.; Bonnet, J.-P. Revisiting and improving the preparation of silicon-based electrodes for lithium-ion batteries: Ball milling impact on poly(acrylic acid) polymer binders. *Mater. Chem. Front.* **2019**, *3*, 881–891. [CrossRef]

11. Mishra, A.; Mehta, A.; Basu, S.; Malode, S.; Shetti, N.; Shukla, S.; Nadagouda, M.; Aminabhavi, T. Electrode materials for lithium-ion batteries. *Mater. Sci. Energy Technol.* **2018**, *1*, 182–187. [CrossRef]

12. Placke, T.; Kloepsch, R.; Dühnen, S.; Winter, M. Lithium ion, lithium metal, and alternative rechargeable battery tech-nologies: The odyssey for high energy density. *J. Solid State Electrochem.* **2017**, *21*, 1939–1964. [CrossRef]

13. Heubner, C.; Liebmann, T.; Lohrberg, O.; Cangaz, S.; Maletti, S.; Michaelis, A. Understanding Component-Specific Con-tributions and Internal Dynamics in Silicon/Graphite Blended Electrodes for High-Energy Lithium-Ion Batteries. *Batter. Supercaps* **2022**, *5*, e202100182. [CrossRef]

14. Choi, J.W.; Aurbach, D. Promise and reality of post-lithium-ion batteries with high energy densities. *Nat. Rev. Mater.* **2016**, *1*, 16013. [CrossRef]

15. Wu, H.; Chan, G.; Choi, J.W.; Yao, Y.; McDowell, M.T.; Lee, S.W.; Jackson, A.; Yang, Y.; Hu, L.; Cui, Y. Stable cycling of double-walled silicon nanotube battery anodes through solid-electrolyte interphase control. *Nat. Nanotechnol.* **2012**, *7*, 310–315. [CrossRef] [PubMed]

16. Zhang, Q.; Yu, Z.; Du, P.; Su, C. Carbon Nanomaterials Used as Conductive Additives in Lithium Ion Batteries. *Recent Patents Nanotechnol.* **2010**, *4*, 100–110. [CrossRef] [PubMed]

17. Drews, M.; Tepner, S.; Haberzettl, P.; Gentischer, H.; Beichel, W.; Breitwieser, M.; Vierrath, S.; Biro, D. Towards 3D-lithium ion microbatteries based on silicon/graphite blend anodes using a dispenser printing technique. *RSC Adv.* **2020**, *10*, 22440–22448. [CrossRef]

18. Liu, W.-R.; Yang, M.-H.; Wu, H.-C.; Chiao, S.M.; Wu, N.-L. Enhanced Cycle Life of Si Anode for Li-Ion Batteries by Using Modified Elastomeric Binder. *Electrochem. Solid State Lett.* **2005**, *8*, A100–A103. [CrossRef]

19. Akbar, A.; Lestari, Y.; Ramadhan, G.; Candra, S.; Sugiarti, E. The Influence of Carboxy Methyl Cellulose (CMC) and So-lution pH on Carbon Fiber Dispersion in White Cement Matrix. *AMM* **2014**, *493*, 661–665. [CrossRef]

20. Lee, J.-H.; Paik, U.; Hackley, V.A.; Choi, Y.-M. Effect of Carboxymethyl Cellulose on Aqueous Processing of Natural Graphite Negative Electrodes and their Electrochemical Performance for Lithium Batteries. *J. Electrochem. Soc.* **2005**, *152*, A1763–A1769. [CrossRef]

21. Lingappan, N.; Kong, L.; Pecht, M. The significance of aqueous binders in lithium-ion batteries. *Renew. Sustain. Energy Rev.* **2021**, *147*, 111227. [CrossRef]

22. Wood, D.L., III; Li, J.; Daniel, C. Prospects for reducing the processing cost of lithium ion batteries. *J. Power Sources* **2015**, *275*, 234–242. [CrossRef]

23. Wenzel, V.; Nirschl, H.; Nötzel, D. Challenges in Lithium-Ion-Battery Slurry Preparation and Potential of Modifying Electrode Structures by Different Mixing Processes. *Energy Technol.* **2015**, *3*, 692–698. [CrossRef]

24. Ding, X.; Liu, J.; Harris, T.A.L. A review of the operating limits in slot die coating processes. *AIChE J.* **2016**, *62*, 2508–2524. [CrossRef]

25. Li, C.-C.; Lin, Y.-S. Interactions between organic additives and active powders in water-based lithium iron phos-phate electrode slurries. *J. Power Sources* **2012**, *220*, 413–421. [CrossRef]

26. Kim, K.; Jeon, W.; Chang, S. Effect of mixing sequences on the electrode characteristics of lithium-ion rechargeable batteries. *J. Power Source* **1999**, *83*, 108–113. [CrossRef]

27. Shaibani, M.; Mirshekarloo, M.S.; Singh, R.; Easton, C.D.; Cooray, M.C.D.; Eshraghi, N.; Abendroth, T.; Dörfler, S.; Althues, H.; Kaskel, S.; et al. Expansion-tolerant architectures for stable cycling of ultrahigh-loading sulfur cathodes in lithium-sulfur batteries. *Sci. Adv.* **2020**, *6*, eaay2757. [CrossRef]

28. Ruschak, K.J. Limiting flow in a pre-metered coating device. *Chem. Eng. Sci.* **1976**, *31*, 1057–1060. [CrossRef]

29. Schmitt, M.; Baunach, M.; Wengeler, L.; Peters, K.; Junges, P.; Scharfer, P.; Schabel, W. Slot-die processing of lithium-ion battery electrodes—Coating window characterization. *Chem. Eng. Process. Process. Intensif.* **2013**, *68*, 32–37. [CrossRef]

30. Kistler, S.; Schweizer, P. *Liquid Film Coating*; Springer: Dordrecht, The Netherlands, 2012.

31. Pallas, N.; Harrison, Y. An automated drop shape apparatus and the surface tension of pure water. *Colloids Surfaces* **1990**, *43*, 169–194. [CrossRef]

32. Mewis, J.; Wagner, N. *Colloidal Suspension Rheology*; Cambridge University Press: Cambridge, MA, USA, 2011.

33. Electrode Resistance Measurement System RM2610, Hioki. Available online: https://www.hioki.com/euro-en/products/resistance-meters/resistance/id_6740 (accessed on 9 July 2023).

34. Grießl, D.; Adam, A.; Huber, K.; Kwade, A. Effect of the Slurry Mixing Process on the Structural Properties of the Anode and the Resulting Fast-Charging Performance of the Lithium-Ion Battery Cell. *J. Electrochem. Soc.* **2022**, *169*, 020531. [CrossRef]

35. Seidl, C.; Thieme, S.; Frey, M.; Nikolowski, K.; Michaelis, A. *Comparison of Electronic Resistance Measurement Methods and Influencing Parameters for Lmfp and High-Nickel Ncm Cathodes*; SSRN: Rochester, NY, USA, 2023.

36. Pahl, M. *Mischen und Rühren*; Wiley-VCH: Weinheim, Germany, 2007.

37. Gordon, R.; Orias, R.; Willenbacher, N. Effect of carboxymethyl cellulose on the flow behavior of lithium-ion battery an-ode slurries and the electrical as well as mechanical properties of corresponding dry layers. *J. Mater. Sci.* **2020**, *55*, 15867–15881. [CrossRef]

38. Ndour, M.; Bonnet, J.-P.; Cavalaglio, S.; Lombard, T.; Courty, M.; Aymard, L.; Przybylski, C.; Bonnet, V. The formulation of a CMC binder/silicon composite anode for Li-ion batteries: From molecular effects of ball milling on polymer chains to consequences on electrochemical performances. *Mater. Adv.* **2022**, *3*, 8522–8533. [CrossRef]

39. Soares, E.J. Review of mechanical degradation and de-aggregation of drag reducing polymers in turbulent flows. *J. Non-Newton. Fluid Mech.* **2020**, *276*, 104225. [CrossRef]

40. Rubinstein, M.; Colby, R. *Polymer Physics*; Oxford University Press: Oxford, UK, 2014.

41. Park, K.; Myeong, S.; Lee, D.; Yoo, H.E.; Kim, J.; Kim, C.; Kim, J.; Sun, S.; Kwon, J.; Kim, S.C.; et al. Improved Li-ion kinetics of the anode by kneading process of binder for lithium-ion batteries with high energy density. *Electrochim. Acta* **2023**, *464*, 142900. [CrossRef]

42. Weber, M.; Moschner, R.; Kwade, A. Modifying the Network Structures of High Energy Anodes for Lithium-Ion Batter-ies through Intensive Dry Mixing. *Energy Technol.* **2022**, *11*, 2200852. [CrossRef]

43. Park, J.; Willenbacher, N.; Ahn, K.H. How the interaction between styrene-butadiene-rubber (SBR) binder and a secondary fluid affects the rheology, microstructure and adhesive properties of capillary-suspension-type graphite slurries used for Li-ion battery anodes. *Colloids Surf. Physicochem. Eng. Asp.* **2019**, *579*, 123692. [CrossRef]